Accepted Manuscript

Geometric calibration of **C**olour **a**nd **S**tereo **S**urface **I**maging **S**ystem of ESA's **T**race **G**as **O**rbiter

Stepan Tulyakov, Anton Ivanov, Nicolas Thomas, Victoria Roloff, Antoine Pommerol, Gabriele Cremonese, Thomas Weigel, Francois Fleuret

Please cite this article as: Tulyakov, S., Ivanov, A., Thomas, N., Roloff, V., Pommerol, A., Cremonese, G., Weigel, T., Fleuret, F., Geometric calibration of **C**olour **a**nd **S**tereo **S**urface **I**maging **S**ystem of ESA's **T**race **G**as **O**rbiter, *Advances in Space Research* (2017), doi: https://doi.org/10.1016/j.asr.2017.10.025

ADVANCES IN SPACE RESEARCH

Geometric calibration of **C**olour **a**nd **S**tereo **S**urface **I**maging **S**ystem of ESA's **T**race **G**as **O**rbiter

Stepan Tulyakov[a,*], Anton Ivanov[a], Nicolas Thomas[b], Victoria Roloff[b], Antoine Pommerol[b], Gabriele Cremonese[c], Thomas Weigel[d], Francois Fleuret[e]

[a]*École Polytechnique Federale de Lausanne, EPFL-ENT-ESC, Station 13, 1015 Lausanne, Switzerland*
[b]*Physics Institute, Space Research and Planetary Sciences, University of Bern, Sidlerstrasse 5, 3012 Bern, Switzerland*
[c]*INAF, Osservatorio Astronomico di Padova, Vicolo Osservatorio 5, 35122 Padova, Italy*
[d]*RUAG Space, RUAG Schweiz AG Schaffhauserstrasse 580, 8052 Zrich, Switzerland*
[e]*Idiap Research Institute, Rue Marconi 19, 1920 Martigny, Switzerland*

Abstract

There are many geometric calibration methods for "standard" cameras. These methods, however, cannot be used for the calibration of telescopes with large focal lengths and complex off-axis optics. Moreover, specialized calibration methods for the telescopes are scarce in literature. We describe the calibration method that we developed for the Colour and Stereo Surface Imaging System (CaSSIS) telescope, on board of the ExoMars Trace Gas Orbiter (TGO). Although our method is described in the context of CaSSIS, with camera-specific experiments, it is general and can be applied to other telescopes. We further encourage re-use of the proposed method by making our calibration code and data available on-line.

*Corresponding author

Email addresses: `stepan.tulyakov@epfl.ch` (Stepan Tulyakov), `anton.ivanov@epfl.ch` (Anton Ivanov), `nicolas.thomas@space.unibe.ch` (Nicolas Thomas), `victoria.roloff@space.unibe.ch` (Victoria Roloff), `antoine.pommerol@space.unibe.ch` (Antoine Pommerol), `gabriele.cremonese@oapd.inaf.it` (Gabriele Cremonese), `thomas.weigel@ruag.com` (Thomas Weigel), `francois.fleuret@idiap.ch` (Francois Fleuret)

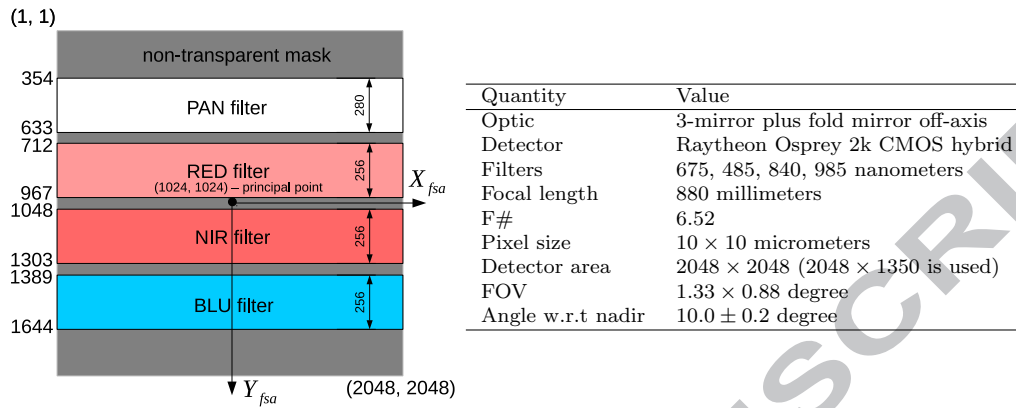| Quantity	Value
Optic	3-mirror plus fold mirror off-axis
Detector	Raytheon Osprey 2k CMOS hybrid
Filters	675, 485, 840, 985 nanometers
Focal length	880 millimeters
F#	6.52
Pixel size	10×10 micrometers
Detector area	2048×2048 (2048×1350 is used)
FOV	1.33×0.88 degree
Angle w.r.t nadir	10.0 ± 0.2 degree

Figure 1: CaSSIS camera specification. The CaSSIS telescope is three-mirror anastigmat system (off-axis) with a fold mirror. The CaSSIS Filter Strip Assembly (FSA) comprises a Raytheon Osprey 2048×2048 hybrid CMOS detector with 4 colour filters mounted on it following the push-frame technique. Narrow dark bands between the filters reduce spectral cross-talk. The detector can acquire an un-smeared image along ground-track. The along-track dimension of the image is then built up and put together on ground.

1. Introduction

On March 15, 2016 Trace Gas Orbiter (TGO) was launched to Mars, as part of the the European Space Agency's (ESA's) ExoMars project. Its aim is to find trace gases, which may be evidence of geological or biological activity on Mars. The Colour and Stereo Surface Imaging System (CaSSIS) is TGO's imaging system that provides visual context for sites identified as potential sources of trace gases. A brief specification of CaSSIS is provided in Tab. 1.

CaSSIS (Thomas et al. 2014; Thomas et al.) is a multi-spectral push-frame camera with 4 rectangular color filters covering its sensor (Fig. 1). As the spacecraft is moving along the orbit, each part of a targeted area becomes visible, sequentially, in each filter. By acquiring and mosaicking multiple images ("framelets"), CaSSIS is able to reconstruct a large 4-colours image of the targeted area.

CaSSIS is also a stereo camera. It is capable of acquiring two images of a target area from two distinct points on the same orbit. While approaching the target area it acquires the first image, then it gets mechanically rotated and acquires the second image, while departing from the target area. By

2

computing parallax from these two images, one can reconstruct a Digital Elevation Model (DEM) of the target area.

To prepare scientific products, such as color images and DEMs from raw CaSSIS images, one needs geometric camera parameters, such as its focal length and a optical distortion model. While their nominal values are known from technical specification, their actual values might deviate from the nominal ones, due to imprecise manufacturing, mounting, or various changes during the spacecraft cruise and operation (due to structure dryout and zero gravity). Therefore, their actual values have to be measured in the controlled environment of the clean room and validated during the commissioning phase in flight. This is the main goal of geometric calibration.

There are many geometric calibration methods (Hartley and Zisserman 2003; Zhengyou 1999; Heikkila and Silven 1997; Tsai 1987) and tools[1,2,3] for "standard" cameras. However, these off-the-shelf tools cannot be used for the calibration of telescopes such as CaSSIS, for two reasons. Firstly, most of these tools require images of calibration targets, such as a checkerboard chart. For telescopes with a large focal length, however, such targets must be very large ($\approx km^2$) and should be placed very far away from the telescope ($\approx 10\ km$), which is impractical. Secondly, telescopes often have off-axis optical designs with complex optical distortion, that cannot be handled by off-the-shelf tools. Therefore, there is a need for specialized calibration methods, which are unfortunately scarce in the literature.

In this paper we describe the calibration method that we developed for CaSSIS. Although our method is described in the context of CaSSIS, it is general and can be applied to other telescopes. We further encourage re-use of the proposed method by making our calibration code and data available on-line[4].

We first discuss in § 2 the related work, and describe in § 3 the geometric camera model adopted in the paper. In § 4 we explain the distortion model selection procedure based on lens simulation, in § 5 we describe the on-ground

---

[1] MATLAB camera calibration tool, https://ch.mathworks.com/help/vision/ug/single-camera-calibrator-app.html, accessed 2017-05-23

[2] OpenCV camera calibration tool, http://docs.opencv.org/2.4/doc/tutorials/calib3d/camera_calibration/camera_calibration.html, accessed 2017-05-23

[3] Caltech camera calibration tool, http://www.vision.caltech.edu/bouguetj/calib_doc/, accessed 2017-05-23

[4] https://github.com/eSpaceEPFL/CASSISgeometry.git

calibration using images of a dotted calibration target captured through a collimator, and in § 6 we describe the in-flight calibration using star field images. Finally, in § 7 we show how refined geometric parameters improve the quality of map-projected CaSSIS images.

2. Related Work

2.1. Optical Distortion models

Off-the-shelf calibration tools typically assume a radial or a Brown-Conrady optical distortion model. The radial model (Hartley and Zisserman 2003) is a simple 5 degrees-of-freedom (DOF) model, only accounting for radially symmetric distortion. Brown-Conrandy (Brown 1966) is a more complex model with 7 DOF, that in addition to the radially symmetric component, accounts for tangential decentering. These models, however, cannot represent the complex distortion in a camera with off-axis optical elements, such as CaSSIS, as we show in § 4. Complex distortion is better modeled by a bi-cubic (Kilpelä 1981) or a rational model (Claus and Fitzgibbon 2005) with 20 and 17 DOF, respectively. In our work we adopted the rational distortion model (discussed in § 3).

2.2. Star field calibration

For geometric calibration of a camera one needs images of calibration targets - objects with known real-world coordinates. Since angular positions of stars are well known and documented in star catalogs[5] , such as Two Micron All-Sky Survey (2MASS) and Tycho-2, star fields can serve as perfect calibration targets. Indeed, star field calibration is widely used in star trackers that are an integral part of every spacecraft (Samaan et al. 2001; Pal and Bhat 2014; Junfeng et al. 2005). The star field calibration can also be used for calibration of consumer-level cameras (Klaus et al. 2004). Unfortunately, all known star field-based calibration methods assume a simplistic optical distortion model, and therefore, cannot be applied for telescope calibration. Before stars from an image can be used for calibration, they should be identified using a star catalog, which fortunately can be done automatically (Lang et al. 2010) with a Astrometry.net library [6].

---

[5]VisieR star catalog library, http://vizier.u-strasbg.fr/, accessed: 2017-05-24

[6]Astrometry.net star recognition tool, http://astrometry.net/, accessed: 2017-05-24

4

3. CaSSIS camera model

The camera model consists of: (1) the intrinsic model, (3) the rational optical distortion model and (3) the extrinsic model. In this section we discuss each part of the camera model in detail.

3.1. Intrinsic Model

The intrinsic model (Hartley and Zisserman 2003, p153-158) describes the transformation from 3D camera frame coordinates $\mathbf{X} = \{X, Y, Z\}$ to 2D image coordinates $\mathbf{x} = \{x, y\}$ as follows:

$$(x, y) = \left(\frac{\mathbf{K}_1^T \mathbf{X}}{\mathbf{K}_3^T \mathbf{X}}, \frac{\mathbf{K}_2^T \mathbf{X}}{\mathbf{K}_3^T \mathbf{X}} \right), \quad \mathbf{K} = \begin{bmatrix} f & 0 & x_0 \\ 0 & f & y_0 \\ 0 & 0 & 1 \end{bmatrix}, \tag{1}$$

where f is the focal length of the camera, measured in pixels, and x_0, y_0 are the coordinates of the principal point in the image. In the case of CaSSIS, we assume that x_0 and y_0 correspond to the center of an image. Therefore, the CaSSIS intrinsic model has only 1 DOF.

3.2. Rational optical distortion model

The intrinsic camera model is complemented with a optical distortion model, that describes the transformation from the distorted image coordinates to the ideal image coordinates. In practice, however a distortion model is often defined in centered focal plane coordinate frame (in case of CaSSIS it is Filter Strip Assembly coordinate frame, shown in Fig. 1). We will follow this convention in our work. As a distortion model we use rational distortion model (Claus and Fitzgibbon 2005):

$$(x_{fsa}, y_{fsa}) = \left(\frac{\mathbf{A}_1^T \chi_\mathbf{6}}{\mathbf{A}_3^T \chi_\mathbf{6}}, \frac{\mathbf{A}_2^T \chi_\mathbf{6}}{\mathbf{A}_3^T \chi_\mathbf{6}} \right), \quad \chi_\mathbf{6} = \begin{bmatrix} i_{fsa}^2 & ij_{fsa} & j_{fsa}^2 & i_{fsa} & j_{fsa} & 1 \end{bmatrix}^T, \tag{2}$$

where $\mathbf{A}_{1...3}^T$ are rows of a 3×6 rational distortion matrix, x_{fsa}, y_{fsa} are ideal coordinates, i_{fsa}, j_{fsa} are distorted coordinates.

The model has several interesting properties. Firstly, although in total the model has 18 parameters, there are only 17 free parameters, since we can always multiply the numerator and the divisor in the 2 by the same number.

5

Secondly, there is no close-form analytical solution for the inverse of the rational distortion model (in other words given the ideal coordinates it is impossible to compute the distorted coordinates analytically). However, the rational model can very precisely represent the inverse of itself (Grompone von Gioi et al. 2010). We use this property and simultaneously estimate two rational models: one that transforms the distorted coordinates to the ideal, and another that transforms the ideal coordinates to the distorted.

Thirdly, the parameters of the rational distortion model can be estimated from single image of a calibration target (up to unknown homography) without knowing the intrinsic and the extrinsic parameters of the camera.

3.3. Extrinsic Model

The extrinsic model (Hartley and Zisserman 2003, p155-156) describes the transformation from the reference (spacecraft) frame coordinates $\mathbf{X_{ref}} = (X_{ref}, Y_{ref}, Z_{ref})$ to the camera frame coordinates $\mathbf{X} = (X, Y, Z)$ as follows

$$\mathbf{X} = \mathbf{R}\mathbf{X_{ref}} + \mathbf{T}, \tag{3}$$

where $\mathbf{R}$ is the 3×3 rotation matrix, and $\mathbf{T}$ is the 3×1 translation vector. The rotation matrix $\mathbf{R}$ is the function of 3 Euler angles $\mathbf{R} = F(\alpha, \beta, \gamma)$. The translation vector is typically ignored, because the camera is much closer to the reference frame than to the scene. The extrinsic model has 3 DOF in total.

4. Distortion model selection

Before CaSSIS was assembled, we were provided with optical distortion data by the telescope manufacturer (RUAG Space Zurich, Switzerland), shown in Tab. 1, computed using a ray-tracing simulation. To find out what distortion model better represented CaSSIS optical distortion, we fitted radial, Brown-Conrady, rational and bi-cubic optical distortion models (see § 2.1) to the data, and compared the average Euclidean error of the models using leave-one-out cross-validation.

The resulting distortion fields and errors for each model are shown in Fig. 2. Simple radial and Brown-Conrady models suffer from more than 1 pixel error, and hence failed to represent the CaSSIS distortion, while bi-cubic and rational models, with less than 0.1 pixel error, performed well. Among

6

	x_{fsa}, [mm]	i_{fsa}, [mm]	y_{fsa}, [mm]	j_{fsa}, [mm]
1	0	0	0	0
2	0	0	-3.3846	-3.3911
3	0	0	-6.7538	-6.7437
4	0	0	3.3846	3.4094
5	0	0	6.7538	6.8165
6	-5.1385	-5.1358	0	0.0022
7	-5.1385	-5.1207	-3.3846	-3.3866
8	-5.1385	-5.1029	-6.7538	-6.737
9	-5.1385	-5.1478	3.3846	3.4093
10	-5.1385	-5.1568	6.7538	6.8142
11	-10.2769	-10.2482	0	0.0089
12	-10.2769	-10.2183	-3.3846	-3.3733
13	-10.3077	-10.2133	-6.7538	-6.7171
14	-10.2769	-10.2722	3.3846	3.4094
15	-10.2769	-10.2901	6.7538	6.8075
16	5.1385	5.1358	0	0.0022
17	5.1385	5.1207	-3.3846	-3.3866
18	5.1385	5.1029	-6.7538	-6.737
19	5.1385	5.1478	3.3846	3.4093
20	5.1385	5.1568	6.7538	6.8142
21	10.2769	10.2482	0	0.0089
22	10.2769	10.2183	-3.3846	-3.3733
23	10.2769	10.183	-6.7538	-6.7173
24	10.2769	10.2722	3.3846	3.4094
25	10.2769	10.2901	6.7538	6.8075

Table 1: The CaSSIS optical distortion data, computed using a ray-tracing simulation. x_{fsa}, y_{fsa} are ideal coordinates and i_{fsa}, j_{fsa} are distorted coordinates in Filter Strip Assembly coordinate frame. Unfortunately, there is no information about precision of the numbers in the table.
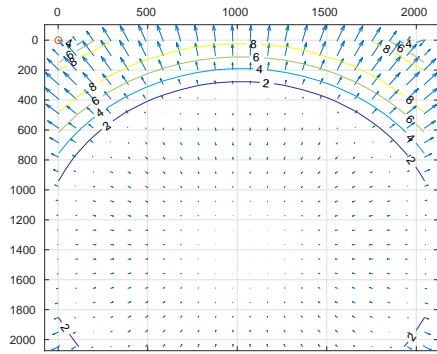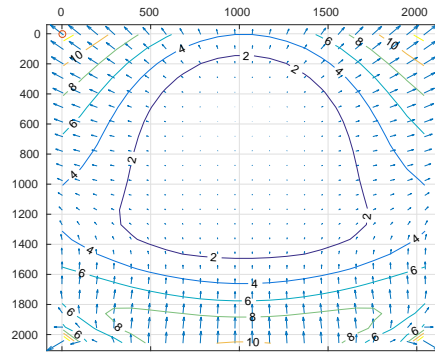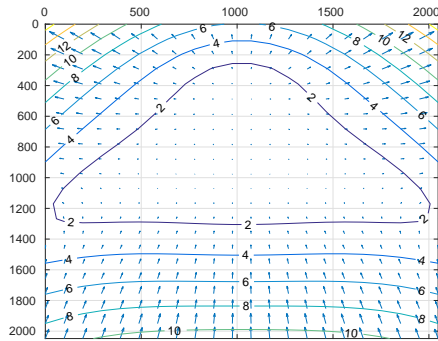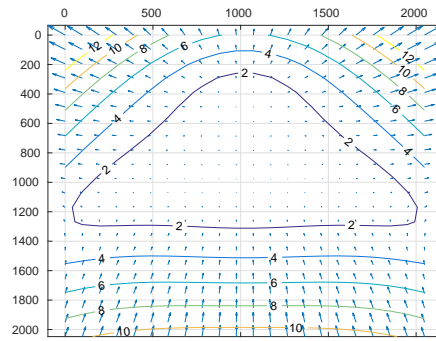
7

(a) radial ($\overline{error}$=3.169 pix)

(b) brown-conrandy ($\overline{error}$=1.585 pix)

(c) rational ($\overline{error}$=0.088 pix)

(d) bi-cubic ($\overline{error}$=0.015 pix)

Figure 2: Distortion models "fitted" to simulated CaSSIS optical distortion data (see Tab. 1). Vectors show the transformation from the distorted to the ideal image. Contour lines show the magnitude of this transformation. The errors are the average Euclidean distances between the positions of the ideal pixels, as predicted by the model, and their actual positions. Note that simple radial (2a) and Brown-Conrady models (2b), with more than 1 pixel error, fail to represent CaSSIS distortion, while bi-cubic (2d) and rational (2c) models, with less than 0.1 pixels error, both perform well.

8

the last two models, we selected the rational model because its parameters can be easily estimated from a single image of a calibration target, moreover it also has less parameters than compared to the bi-cubic model (the rational model has 17, whereas the bi-cubic model has 20 free parameters).

5. On-ground calibration

After the CaSSIS camera was assembled and tested, we attempted to estimate the distortion model from a single image of a dotted calibration target, as in Claus and Fitzgibbon 2005. Because the focal length of CaSSIS is too large to acquire in-focus images of the target from a reasonable distance, we used a set-up with a collimator (Fig. 4).

After the image was acquired, we applied adaptive thresholding and connected components detection methods to identify dots in the image. Then, we found the dot centers using a centroid algorithm. Finally, we fitted the regular rectangular grid to the dot centers, using a simple algorithm that starts from an arbitrarily-selected dot, and expands the grid in horizontal and vertical directions, until no new dots can be added to the grid.
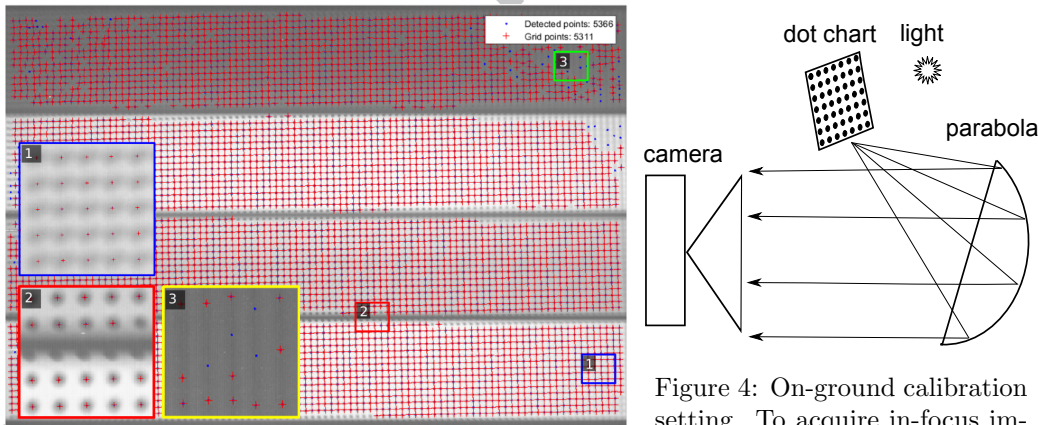

Figure 3: Image of the dotted target overlaid with the fitted grid (blue filter on the top). Red crosses show dots that were added to the grid. Blue points show dots, that were not added to the grid.

Figure 4: On-ground calibration setting. To acquire in-focus image of the dotted calibration target from a reasonable distance, we put it in the focus of the parabolic collimator.

The acquired image with the fitted grid is shown in Fig. 3. Analysis of the grid confirmed the presence of a small optical distortion in the image: the grid rows and columns appeared, not as straight lines but, as high-order curves.

9

However, we failed to estimate the distortion field resembling Fig. 2c using the grid. This is probably due to the fact that the experimental data was contaminated with residual distortion coming from the off-axis collimator. If we knew the distortion of the collimator, we could have attempted to decouple them. However, this was not the case.

6. In-flight calibration

During TGO commissioning and mid-cruise checkout, CaSSIS acquired multiple images of star fields, that we used for in-flight calibration. In § 6.1 we describe our in-flight calibration method and in § 6.2 we show the calibration results.

6.1. Method

.5 The overall work flow for in-flight calibration is shown in Fig. 5 and each individual procedure is described below. They are performed in that order.

Image assembly. We assemble full-sensor images from several data packets according to information in XML files from the telemetry conversion (Each image is accompanied by housekeeping data)

Figure 5: Work flow of the in-flight calibration. Ellipses show the input and the output data and rectangles show processing steps.

De-noising and flattening. We denoise every image by subtracting the median of several images from each image. This procedure helps us to get rid of fixed-pattern noise and hot pixels. Then we flatten each image by applying a Difference-of-Gaussian (DoG) filter.

Star field recognition. We perform star detection and recognition using the open-source Astrometry.net library and Two Micron All-Sky Survey star catalog (2MASS). The library takes an image of a star field as an input, and outputs (x, y) coordinates of stars in the image, and their corresponding (Ra, Dec) coordinates in equatorial frame (and epoch) J2000. Note, that we do not take into account proper motion of stars in our work. This cause
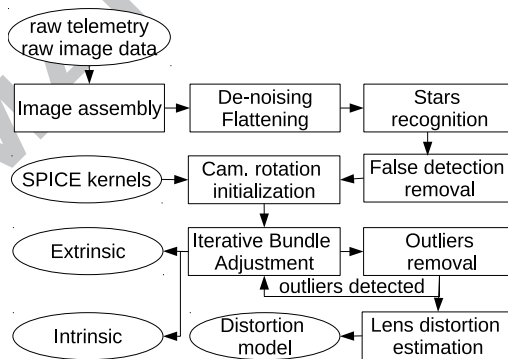
10

error when we project stars to the sensor. The magnitude of the error can be approximated as following

$$tan((year - 2000)\mu)f/p, \qquad (4)$$

where μ is a typical proper motion per year, f is a camera focal length and p is a pixel pitch. With a typical proper motion equal to $\mu \approx 0.1$ arc-seconds per year, typical error will be about 0.7 pixels.

False detections removal. In the next step we collect information about detected stars from all images and filter out erroneous detections. Since the calibration image sets consist of sequences of 3-4 almost identical images, we mark a star as a false detection, if it is not re-detected at a similar position in at least 2 images.

Camera rotation initialization. We find the camera rotation for every image independently. During the estimation, we set the focal length of the camera to nominal and search for the camera rotation that minimizes the projection error, i.e the Euclidean distance between observed and predicted star positions in each image individually. The optimization is done with LevenbergMarquardt algorithm (lsqnonlin in MATLAB). We initialize the optimization with rotation angles from the SPICE kernel[7,8]. The SPICE kernels contain information about orientation and position of spacecraft and its elements, received from its sensors for any moment in time.

Iterative Bundle Adjustment (BA). In this step we search for a refined focal length and rotations that minimize the projection errors for all images simultaneously. The optimization is performed with LevenbergMarquardt algorithm. We initialize the optimization with the focal length and rotation matrices we found in the previous step. After each BA iteration, stars that have large residual projection errors compared to their spatial neighbors are rejected as outliers and BA is performed again until no new outliers are found. Without this outlier rejection, the subsequent optical distortion estimation would fail.

---

[7]ExoMars Trace Gas Orbiter SPICE kernels, https://naif.jpl.nasa.gov/pub/naif/EXOMARS2016, accessed: 2017-05-24

[8]SPICE toolkit, https://naif.jpl.nasa.gov/naif/toolkit.html, accessed: 2017-05-24

11

Rational optical distortion estimation. In this step we "freeze" the intrinsic and the extrinsic camera models and search for a rational optical distortion model that minimizes the remaining projection error. The optimization is performed with LevenbergMarquardt algorithm. We initialize the optimization process using a "no distortion" hypothesis.

6.2. Results

We performed our experiments on 3 datasets: "mcc motor" and "pointing cassis" both acquired in July 2016 during mid-cruise checkout, and "commissioning2", acquired on April 2016 during near-Earth commissioning. We selected these datasets, since they contain images of dense star fields acquired with long 1.92-second exposures. We estimated the camera parameters using the combined "mcc motor" and "pointing cassis" set, which we called the *training set*, and validated the results on "commissioning2" set, which we called the *validation set.*

A number of images and the recognized stars in every set are shown in Tab. 2. As shown in Fig. 6, the stars from the training set cover the sensor densely and uniformly, allowing for good optical distortion estimation.

Data	Name	No. images	No. stars
2016-04-13	pointing cassis	45	539
2016-06-14	mcc motor	92	2573
2016-04-07	commissioning 2	12	670

Table 2: Datasets summary. Note that sets consist of sequences of 3-4 almost identical images, acquired within short time interval. There are 10-60 stars in each image.
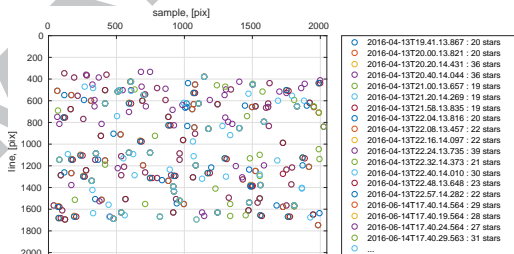

Figure 6: Position of all stars detected in combined "mcc motor" + "pointing CaSSIS" set on the detector. Note that the detector is almost uniformly filled. On the top and the bottom parts of the sensor we do not have observations, since they are covered by non-transparent mask.

Using stars detected in the training set, we refined the camera rotations obtained from SPICE kernels for every image individually, while keeping the focal length of the camera fixed to the nominal. By refining the rotations, we reduced the mean Euclidean distance between observed and the predicted star positions in training-set images from 2471.14 (median 147.89) to 4.09 pixels. The initial mean distance is very large due to several anomalies in rotation sensor readouts..

Then, we used the estimated camera rotations and the nominal focal length to initialize the iterative bundle adjustment process that refined the

(a) 1st BA iteration

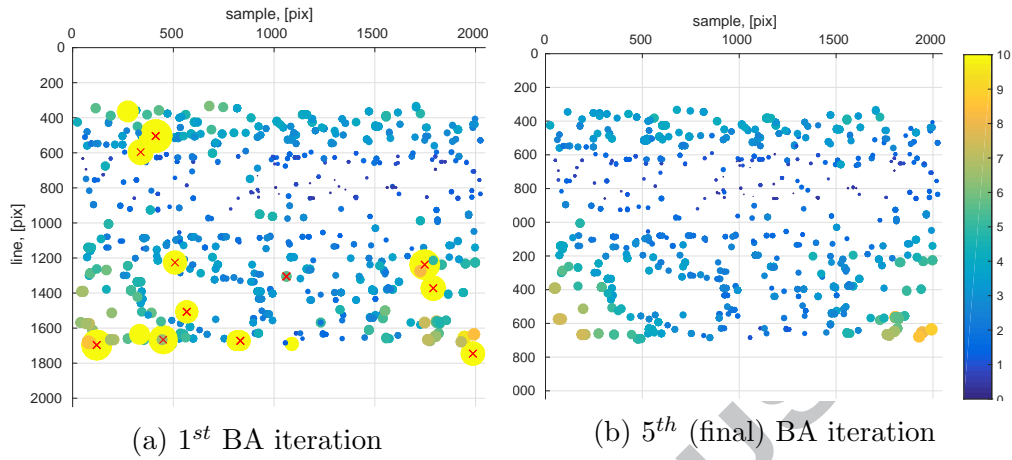(b) 5th (final) BA iteration

Figure 7: Residuals after the first and the fifth BA iterations in the detector coordinate frame. Color coding shows the actual scale of the residuals. Crossed-out residuals correspond to the identified outliers. On the top and the bottom parts of the sensor we do not have observations, since they are covered by a nontransparent mask. Note that after the first iteration (7a), the residuals contain gross outliers, while after the fifth iteration (7b) residuals form a clear spatial pattern suggesting the presence of optical distortion. The average Euclidean error before BA is 4.09 pixels, after the first iteration it is 3.26 pixels, and after the fifth iteration it is 2.56 pixels.

(a) from star field images
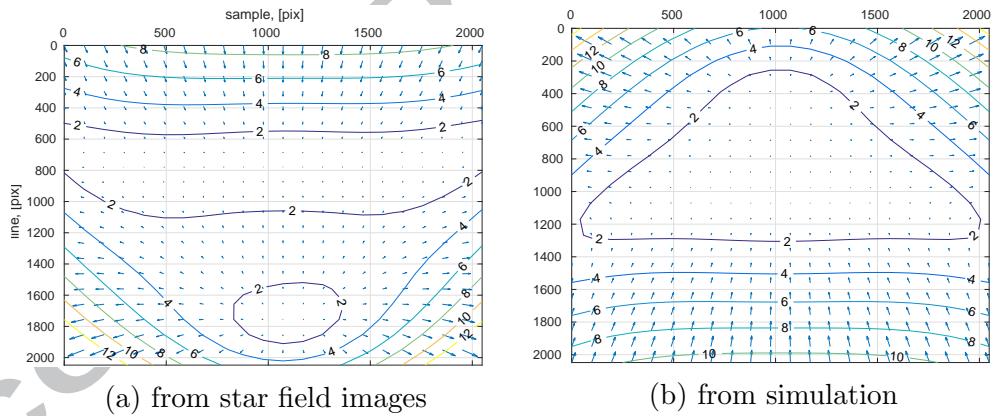
(b) from simulation

Figure 8: The distortion field estimated from star field images in the detector coordinate frame (8a) and optical simulations (8b), described in §4. Vectors show transformation from distorted to ideal image. Contours show magnitude of the transformation. Note that the distortion fields are very similar in shape, with an apparent 180 degree rotation and vertical translation.

13

camera rotations and focal length using all images simultaneously, while ignoring optical distortion. The iterative bundle adjustment converged after 6 iterations. The effect of the iterative outliers rejection scheme is shown in Fig. 7. Note that after the first iteration, the BA residuals contain gross outliers, while after the last iteration, the residuals form a clear spatial pattern suggesting the presence of optical distortion. BA reduced the average Euclidean distance between observed and predicted star positions in the training set images from 4.09 to 2.56 pixels. The refined focal length was found by BA to be 875.96 millimeters, i.e. slightly shorter than the nominal focal length of 880 millimeters.

Then, we "froze" the focal length and camera rotations and estimated the rational distortion model.

The estimated distortion field is shown in Fig. 8a. Note that its shape resembles the distortion field obtained by fitting the rational model to lens simulation data in §4, duplicated for convenience in Fig. 8b, with an apparent 180 degree rotation and vertical translation of the field as the most obvious difference. The rotation is probably caused by the particular sensor mounting with respect to the lens.

Parameters of the estimated distortion model are shown in Tab. 3. The distortion model fitting reduced the average Euclidean distance between the observed and the predicted star positions in the training set images from 2.56 to 0.67 pixels. Moreover, as shown in Fig. 9, the residuals after fitting the optical distortion model became spatially uniform and small when compared to the bundle adjustment residuals from Fig. 7b. Appar-
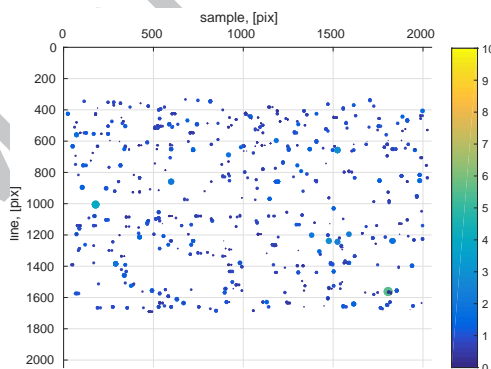

Figure 9: Residual errors in pixels after optical distortion estimation in detector coordinate frame. The average error is 0.67 pixels. Color coding shows the actual error scale, that is similar to Fig. 7b. Note that the errors are small and spatially more uniform than compared to the residual errors after BA from Fig. 7b. Apparent absence of a spatial pattern in the remaining residuals probably suggests that the remaining residual error is caused by some spatially uniform error.

ent absence of a spatial pattern in the remaining residuals probably suggests that they are caused by some spatially uniform error, such as, for example, stars coordinate estimation error or error due to proper motion (see §6.1). Interestingly, average magnitude of the remaining residuals is very close to

14

the expected error from the proper motion.

Finally, we computed the error of the estimated camera model on a separate validation set, that was not used for model estimation, while effectively ignoring extrinsic model. With the refined camera model, the average projection error is 0.47 pixels, while with the nominal camera

A11	A12	A13	A14	A15	A16
0.0038	-0.0134	0.0000	1.0002	-0.0004	-0.0009
A21	A22	A23	A24	A25	A26
-0.0001	0.0037	-0.0133	-0.0002	0.9953	-0.0184
A31	A32	A33	A34	A35	A36
0.0000	0.0000	0.0000	0.0037	-0.0142	1.0000

Table 3: Parameters of the rational distortion model from § 3.2, estimated using star field images.

model the error would be 3.42 pixels. This result suggests that our geometric calibration results are valid.

7. Colour image experiment

A month after TGO's Mars orbital insertion, CaSSIS captured several colour images of Mars from the elliptic capture orbit. In order to verify the effectiveness of our calibration, we map-projected these images using the nominal and the refined geometric models, and compared the quality of the resulting images. The map-projection was performed using Integrated Software for Imagers and Spectrometers (ISIS)[9]. In § 7.1 we describe the work flow of our color image experiment, and in § 7.2 discuss the results.

7.1. Method

The work flow of the colour image experiment is shown in Fig. 10, with each individual procedure described below.

First of all, all data packets belonging to a particular sequence and a color band are extracted from the dataset. Next, we correct the optical distortion in every data packet. Then, we convert each data packet to ISIS ".cub" format (*cassis2isis*) and add information from the SPICE kernel to each ".cub" (*spiceinit*).

After that, we compute optimal pixel resolution for the whole sequence (*mosrange*). Then we project all ".cub" that correspond to a single band of a image sequence into a sinusoidal map (*cam2map*), while keeping the pixel resolution equal to the optimum resolution. Next, we mosaic all projected

---

[9]USGS Integrated Software for Imagers and Spectrometers, https://isis.astrogeology.usgs.gov, accessed: 2017-06-06

".cub" into one image, corresponding to a single band of the sequence (*automos*). We repeat the process described above for every color band. After that, from all bands we crop out common area, visible in all color bands (*maptrim*). This is required since "by default" map projection of every band has its own coordinate limits. Finally, we combine the individual color bands into a multi-band cube (*cubeit*).

7.2. Results

During our experiments we noticed that map-projected images of individual color bands were misaligned along the track by 1-10 pixels, depending on the sequence. This fact, possibly caused by the off-nadir pointing of the camera relative to its rotation axis being slightly different from the nominal. This fact needs to be properly investigated. Meanwhile we checked the validity of the optical distortion model by verifying that the color band images are distortion-free. For that we compensated color band misalignment with a simple shift and compared color band images.
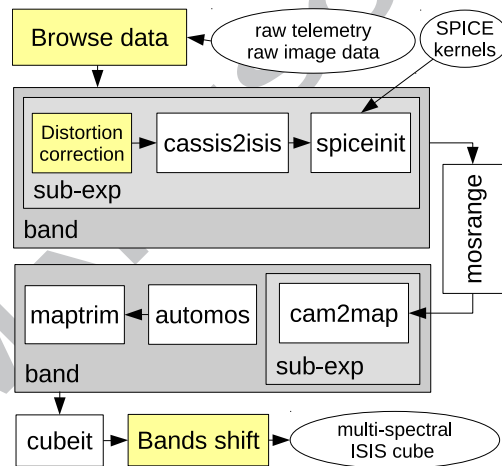

Figure 10: Work flow of the color image experiment. Ellipses represent data, white rectangular boxes represent the standard ISIS functions, and yellow boxes represent the scripts implemented in Python.
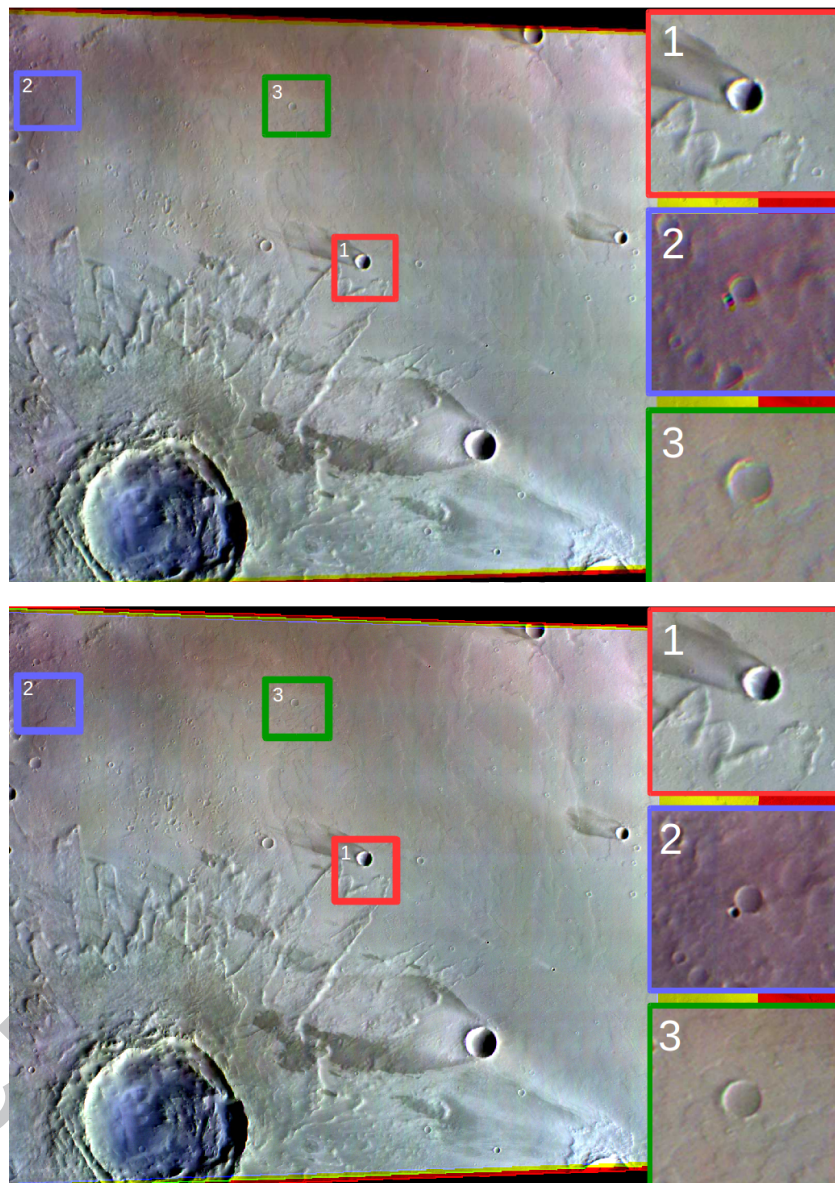
The results of this comparison are shown in Fig. 11. As seen from the figure, when we use nominal camera parameters, the projected image (first) has color fringes (close-up #1, 2 and 3) and stitching artifacts (close-up #3), whereas when we use refined parameters, the projected image (second) is almost perfect.

This confirms that the developed calibration method works and improves the quality of the final scientific products.

8. Conclusion

In this paper we developed a method for geometric calibration of telescopes with large focal length and complex optical distortion. The proposed method was used to refine the nominal parameters of the CaSSIS camera on board

16

Figure 11: Map projection of a CaSSIS image (first "framelet" acquired on November 22, 2016 at 16:01:10, central $(lat, lon) = (-9.03, 218.49)$). Images are shown in false colour (RED $\rightarrow$ red, NIR $\rightarrow$ green, BLU $\rightarrow$ blue channel). On-ground resolution is 35.52 meters/pixel. Color bands are aligned as described in §7.2. Note that when we use nominal camera parameters, the projected image (first) has color fringes (close-up #1, 2 and 3) and stitching artifacts (close-up #3), while when we use refined parameters, the projected image (second) is almost perfect. Some prominent artifacts in the form of vertical and horizontal banding over the image are due to incorrect photometric calibration, and not to incorrect geometric calibration. This issue is investigated independently.

17

ESA's TGO. As a result, we were able to improve the quality of scientific products, such as color images.

Our method is general and can be used for the calibration of other telescopes. We further encourage re-use of the proposed method by making our calibration code and data available on-line.

Acknowledgements

References

Brown, D., 1966. Decentering Distortion of Lenses. Photogrammetric Engineering 32, 444–462.

Claus, D., Fitzgibbon, A.W., 2005. A rational function lens distortion model for general cameras, in: Proceedings of the IEEE international conference on Computer Vision and Pattern Recognition (CVPR), pp. 213–219.

Grompone von Gioi, R., Monasse, P., Morel, J.M., Tang, Z., 2010. Self-consistency and universality of camera lens distortion models. CMLA Preprint, ENS-Cachan.

Hartley, R., Zisserman, A., 2003. Multiple View Geometry in Computer Vision. Cambridge University Press.

Heikkila, J., Silven, O., 1997. A four-step camera calibration procedure with implicit image correction, in: Proceedings of the IEEE Computer Vision and Pattern Recognition (CVPR), 1997, pp. 1106–1112.

Junfeng, X., Wanshou, J., Jianya, G., 2005. On-orbit Stellar Camera Calibration Based on Space Resectioning, in: Proceedings of the IEEE Congress of International Society for Photogrammetry and Remote Sensing Proceedings (ISPRS).

Kilpelä, E., 1981. Compensation of systematic errors of image and model coordinates. Photogrammetria 37, 15–44.

Klaus, A., Bauer, J., Karner, K., Elbischger, P., Perko, R., Bischof, H., 2004. Camera calibration from a single night sky image, in: Proceedings of the IEEE international conference on Computer Vision and Pattern Recognition (CVPR), pp. I–I.

Lang, D., Hogg, D.W., Mierle, K., Blanton, M., Roweis, S., 2010. Astrometry.net: Blind astrometric calibration of arbitrary astronomical images. The astronomical journal 139, 1782.

Pal, M., Bhat, M.S., 2014. Autonomous Star Camera Calibration and Spacecraft Attitude Determination. Journal of Intelligent & Robotic Systems .

19

Samaan, M., Griffth, T., Singla, P., Junkins, J.L., 2001. Autonomous on-orbit calibration of star trackers, in: Proceedings of the IEEE Core Technologies for Space Systems Conference (Communication and Navigation Session).

Thomas, N., Cremonese, G., Ziethe, R., Gerber, M., Brndli, M., Bruno, G., Erismann, M., Gambicorti, L. Gerber, T., Ghose, K., Gruber, M., Mischler, H., Jost, J., Piazza, D., Pommerol, A., Rieder, M., Roloff, V., Servonet, A., Trottmann, W., Uthaicharoenpong, T., Zimmermann, C., Vernani, D., Johnson, M., Pel, E., Weigel, T., Viertl, J., Roux, N., Lochmatter, P., Sutter, G., Casciello, A., Hausner, T., Ficai Veltroni, I., Da Deppo, V., Orleanski, P., Nowosielski, W., Zawistowski, T., Szalai, S., Sodor, B., Tulyakov, S., Troznai, G., Banaskiewicz, M., Bridges, J., S., B., Debei, S., El-Maarry, M., Hauber, E., Hansen, C., Ivanov, A., , Keszthelyi, L., Kirk, R., Kuzmin, R., Mangold, N., Marinangeli, L., Markiewicz, W., Massironi, M., McEwen, A., Okubo, C., Tornabene, L., Wajer, P., J.J., W., . The Color and Stereo Surface Imaging System (CaSSIS) for ESA's Trace Gas. Submitted to Space Science Reviews .

Thomas, O.N., Cremonese, G., Banaszkiewicz, M., Bridges, J., Byrne, S., Da Deppo, V., Debei, S., El-Maarry, M.R., Hauber, E., Hansen, C.J., Ivanov, A., Markiewicz, W., Massironi, M., Mcewen, A.S., Okubo, C., Orleanski, P., Pommerol, A., Wajer, P., Wray, J., 2014. The Color and Stereo Surface Imaging System (CaSSIS) for ESA's Trace Gas, p. 1067.

Tsai, R., 1987. A versatile camera calibration technique for high-accuracy 3d machine vision metrology using off-the-shelf tv cameras and lenses. IEEE Journal on Robotics and Automation 3, 323–344.

Zhengyou, Z., 1999. Flexible camera calibration by viewing a plane from unknown orientations, in: Proceedings of the IEEE International Conference on Computer Vision (ICCV), 1999, pp. 666–673.

Highlights

- A general method for geometric calibration of telescopes with off-axis optics is proposed.

- The method is successfully applied for calibration of CaSSIS on-board of ESA's ExoMars TGO.

- The method is shown to improve quality of the scientific products.